Advanced Functional Materials

ADVANCED FUNCTIONAL MATERIALS
www.afm-journal.de

RESEARCH ARTICLE

Amorphous Structure Engineering for Fabricating Highly Efficient Eu^{2+}-Doped Red-Emitting Luminescent Glass Ceramics

Shuangyin Zhu[1] | Xinyue Li[2] | Junyi Du[3] | Shisheng Lin[1] | Lingwei Zeng[4] | Longkun Zhan[2] | Qin Xu[2] | Xvsheng Qiao[5] | Jidong Lin[1] | Daqin Chen[1,6]

[1]College of Physics and Energy, Fujian Normal University, Fuzhou, P. R. China | [2]College of Materials and Environmental Engineering, Hangzhou Dianzi University, Hangzhou, P. R. China | [3]School of Materials Science and Engineering, Qilu University of Technology, Jinan, P. R. China | [4]School of Chemistry and Chemical Engineering, Key Laboratory of Theoretical Organic Chemistry and Functional Molecule of Ministry of Education, Hunan University of Science and Technology, Xiangtan, P. R. China | [5]State Key Laboratory of Silicon Materials &, School of Materials Science and Engineering, Zhejiang University, Hangzhou, P. R. China | [6]Fujian Provincial Engineering Technology Research Center of Solar Energy Conversion and Energy Storage, Fuzhou, P. R. China

Correspondence: Xinyue Li (lixy@hdu.edu.cn) | Shisheng Lin (linshisheng@fjnu.edu.cn) | Daqin Chen (dqchen@fjnu.edu.cn)

Received: 23 March 2026 | **Revised:** 2 June 2026 | **Accepted:** 15 June 2026

Keywords: glass ceramics | laser-driven lighting | LED | rare earth luminescent materials

ABSTRACT

Eu^{2+}-doped red-emitting color converters are extremely scarce and often exhibit limited photoelectric performance and thermal stability under high-flux solid-state lighting (SSL) conditions, primarily due to imprecise control of Eu^{2+} site occupancy and the lack of a robust protective matrix. In this work, high-performance red-emitting $Mg_2Al_4Si_5O_{18}$ (MAS): Eu^{2+} glass-ceramics (GCs) were developed via amorphous structure engineering. This composite material demonstrates a high crystallinity of 98.2%, an internal quantum yield (IQE) of 99.8%, an external quantum yield (EQE) of 73.2%, and an integrated luminescence intensity loss of only 7.0% at 423 K, presenting competitive overall performance in state-of-the-art red-emitting color converters. Further, the broad applicability and potential of the MAS: Eu^{2+} GCs in lighting applications were verified through the fabrication of high-quality light-emitting diodes (LEDs) excited by violet chips and blue laser-driven lighting systems. This study provides systematic guidance for the targeted development of Eu^{2+}-doped luminescent materials, particularly Eu^{2+}-doped GCs, and contributes to the development of next-generation lighting technologies.

1 | Introduction

To date, color rendering performance and energy efficiency of solid-state lighting (SSL) technology have achieved remarkable advances to satisfy the ever-growing demand for high-quality illumination [1–3], with red-emitting color converters well-recognized for compensating red spectral deficiencies, boosting overall performance, and enabling high color rendering index (CRI) [4–6]. Despite significant progress enabled by mainstream commercial red emitters (nitrides such as (Ca, Sr)$AlSiN_3$: Eu^{2+}, abbreviated as CSASN: Eu^{2+} and fluorides such as K_2SiF_6: Mn^{4+}), they are severely limited by high synthesis costs for nitrides and poor stability as well as low thermal quenching resistance for fluorides [7, 8]. As such, there has been continuous research conducted on alternative red-emitting color converters, among which glass-ceramic (GC) composites stand out as promising candidates due to their bulk morphology, excellent thermal stability, and robust structural stability [9, 10]. However, the coupling of glass network design and crystallization kinetics increases the difficulty of precise activator site engineering,

which is essential for optimizing quantum yield and emission purity.

For GC composites, luminescent performance depends on the in-situ precipitation of target crystalline phases in the glass matrix, accompanied by the effective migration and selective site occupancy of Eu^{2+} activators [11–13]. In fact, the SiO_2-MgO-Al_2O_3 system is an ideal candidate for Eu^{2+}-activated red-emitting materials, with a favorable aluminosilicate-based composition favoring glass network formation and subsequent in-situ crystallization [14–16]. The corresponding $Mg_2Al_4Si_5O_{18}$ (MAS, α-cordierite) phase exhibits a unique hexagonal structure (space group: *P*6/*mcc*, No. 192), possessing two types of [MgO_6] polyhedral sites and interstitial channel sites, which can effectively accommodate Eu^{2+} ions [17–19]. Notably, MAS: Eu^{2+} in the phosphor form generally exhibits broadband blue emission, while the MAS: Eu^{2+} GCs exhibit pure red emission. This red emission is often attributed to the preferential occupancy of Eu^{2+} at interstitial channel sites [20–22]. However, the exact origin remains a subject of academic debate, as other studies have suggested that Eu^{2+} ions substituted at potential [MgO_6] sites may also contribute significantly to the red emission [23]. Given these conflicting viewpoints, the fine regulation of the glass network structure and its impact on the site-selective occupancy of Eu^{2+} remain underexplored, indicating considerable potential for further luminescence optimization.

Herein, amorphous structure engineering is employed to fabricate high-performance red-emitting MAS: Eu^{2+} GCs. The precise modulation of the Al_2O_3 content (Al/Si ratio) is not merely a compositional change but also a fundamental determinant of the glass skeleton polyhedra (Q_n) and non-bridging oxygen density. It can trigger the Al/Si rearrangement within the MAS lattice and encourage Eu^{2+} ions to preferentially occupy the interstitial channel sites, thus resulting in pure red emission at 620 nm. This glass-network modification established a MAS-like topology, thus achieving a remarkable crystallinity of up to 98.2%. The composite exhibited an internal quantum yield (IQE) of 99.8%, an external quantum yield (EQE) of 73.2%, and a minimal luminescence loss of 7.0% at 423 K, demonstrating competitive performance compared to previously reported red-emitting converters. Moreover, MAS: Eu^{2+} GCs demonstrated robust performance in violet-chip light-emitting diodes (LEDs) and blue-laser-driven lighting systems. These findings provide systematic insights into the rational design of Eu^{2+}-doped luminescent GCs, contributing to the development of next-generation SSL.

2 | Results and Discussion

2.1 | Glass Crystallization, Structural, and Optical Characterizations

The SiO_2–MgO–Al_2O_3 ternary phase diagram in Figure 1a shows the cordierite phase area in the Al–Si-rich region [24], where its broadly tunable Al content facilitates lattice engineering regulation through in-situ crystallization. As such, in order to investigate the effects of the Al/Si ratio on the structure and properties of cordierite-based glass/GC composites, a series of 60SiO_2-$x$$Al_2O_3$-30MgO-$y$$Eu_2O_3$ (in mol%, x = 20−37, y = 0.5−2.5) compositions were designed to fabricate MAS: Eu^{2+} GC composites (denoted as PG20−PG37 for precursor glasses and GC20−GC37 for GCs). Differential scanning calorimetry (DSC) analysis identified the optimal crystallization temperature of PG to be approximately 1047°C, at which heat treatment effectively precipitated the MAS phase (JCPDS No. 84–1219) for PG20 (Figure S1). As demonstrated from Figure 1b, Al/Si atoms predominantly occupy tetrahedral sites within the MAS crystal structure: [Al1/Si1O_4] (T1) edge-shares with [MgO_6] octahedra, while [Al2/Si2O_4] (T2) corner-shares to form six-membered rings along the *c*-axis, and adjacent rings are interconnected through [Al1/Si1O_4] and [MgO_6] units, thus creating Mg^{2+} lattice sites and interstitial channels (within the six-membered rings) that are conducive to Eu^{2+} doping [23].

For the representative PG20, Eu^{2+} in its amorphous glass structure exhibits typical broad excitation and emission bands from 4f-5d transitions (Figure S2), while the in-situ crystallized GC20 shows a broad asymmetric emission spectrum with two peaks at 470 and 605 nm (Figure 1c). The significant differences in photoluminescence excitation (PLE) spectra and luminescent decay curves confirm that these emissions originate from different luminescent centers (Figure S3) [25]. Notably, at a fixed Eu^{2+} concentration, the increased Al_2O_3 content in the GC effectively suppresses the blue emission at 470 nm, significantly enhances the red emission, and gradually redshifts the emission peak from 605 to 619 nm (Figure 1d; Figure S4). Inductively coupled plasma optical emission spectrometry (ICP-OES) analysis reveals that the Eu concentrations of the GC20 and GC34 samples differ by less than 4%, indicating negligible activator loss during glass melting and subsequent crystallization, and excluding concentration-related interference with luminescence (Table S1, Note S1). Accordingly, formation energy calculations reveal that increasing Al_2O_3 content more substantially reduces the formation energy of Eu^{2+} incorporation into six-membered ring sites than that associated with substitution at [MgO_6] sites, which promotes its preferential occupancy and thus enhances red emission (Figure 1e; Note S2, Table S2).

Upon optimization, a pure red-light emission centered at 620 nm was successfully achieved for GC34 under 420 nm excitation (Figure 1f). In addition, the optimal Eu^{2+} concentration for GC34 is determined to be y = 1.5 mol%, with a broad excitation band extended from the ultraviolet to the blue region (Figure S5). Concurrently, the Rietveld refinement results confirm the high phase purity of the crystallized GC34, yielding an exceptionally high crystallinity of up to 98.2%. Subsequently, multi-scale structural characterizations encompassing scanning electron microscopy (SEM) gradient etching analysis and transmission electron microscopy (TEM) investigations collectively corroborate the pervasive, matrix-wide high crystallinity and excellent structural uniformity of the GC34 sample (Note S3 and Figures S6–S8). However, excessive Al_2O_3 addition ($x \geq 35$ mol%) results in the detectable formation of a mullite impurity phase coexisting with the original MAS phase (Figure S9), which is highly likely correlated with an undesired increase in blue emission [26]. x-Ray absorption near-edge structure (XANES) analysis at the Eu L_3-edge unequivocally confirmed the exclusive presence of Eu^{2+} in GC20 and GC34, demonstrating that the Eu ions were adequately reduced to the divalent state during sample preparation (Figure 1g). The quantum yield of GCs reached its maximum at GC34 (IQE = 99.8%, EQE = 73.2%), attributed

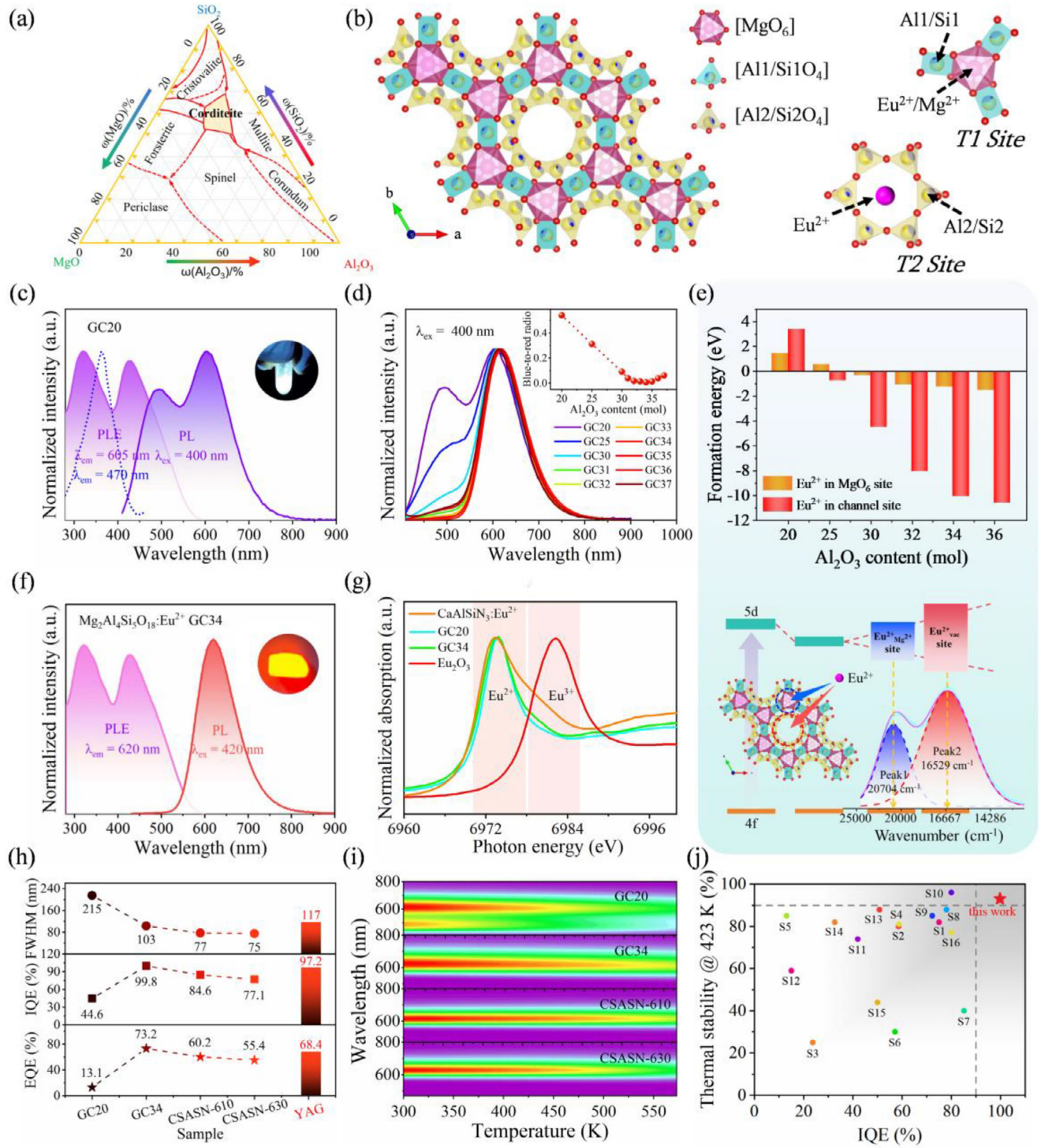

FIGURE 1 | Structural analysis and optical characterization of MAS: Eu^{2+} GCs. (a) Ternary phase diagram of the SiO_2–MgO–Al_2O_3 system. (b) Hexagonal MAS crystal structure viewed along the *c*-axis, with [MgO_6] octahedra and interstitial ring channels indicated as possible Eu^{2+} sites. (c) PLE and PL spectra of GC20. (d) PL spectra of GCs with different Al_2O_3 contents; inset: blue/red emission intensity ratio. (e) Formation energies of Eu^{2+} substitutions in MgO_6 and six-membered rings, together with the schematic 5d-4f energy level diagram of Eu^{2+} in MAS GC. (f) PLE and PL spectra of GC34. (g) Eu L_3-edge XANES spectra of GC20 and GC34, along with reference CSASN: Eu^{2+} and Eu_2O_3. (h) FWHM, IQE, EQE, take YAG as the reference standard and (i) 2D contour plots of temperature-dependent PL for GC20, GC34, CSASN-610, and CSASN-630. (j) IQE and thermal stability summary of representative red-emitting phosphors.

to enhanced radiative transitions and suppressed non-radiative processes (Note S4 and Figures S10–S13) [27], and compared to commercial CSASN: Eu^{2+}, GC34 exhibited a larger full width at half maximum (FWHM = 103 nm) and higher quantum yield under violet excitation (420 nm) (Figure 1h, Figures S14 and S15). Meanwhile, cross-validation using a commercial benchmark $Y_3Al_5O_{12}$: Ce^{3+} (YAG: Ce^{3+}) phosphor yielded efficiency data in line with the manufacturer's specifications, ensuring the reliability of these results (Figure S16) [28]. In terms of thermal stability, GC34 retains 93.0% of its initial emission intensity at 423 K, which is comparable to CSASN: Eu^{2+} phosphors and superior to GC20 (Figure 1i; Figures S17 and S18). Overall, as depicted in Figure 1j and Table S3, the MAS: Eu^{2+} GC34 exhibits highly competitive comprehensive performance among reported red-emitting color converters. This prominent standing is collectively underpinned by its highly crystalline phase, suppressed defect states, and optimized Eu^{2+} site occupancy.

2.2 | Topology Engineering for Site-Selective Occupation of Eu^{2+}-Activators

To elucidate the regulatory effect of Al_2O_3 content on the amorphous network structure at the atomic scale, the distribution of Si and Al Q_n structural units is initially computed through molecular dynamics (MD) simulation (Figure 2a). Increasing the Al_2O_3 content from 20 to 34 mol% significantly elevates the proportion of highly polymerized Q_4 units, with Si-Q_4 rising from ~65% to ~73%, while Al-Q_4 remains high at approximately 72%. However, the proportions of low-polymerized Q_1, Q_2, and Q_3 units decrease correspondingly, reflecting enhanced amorphous network polymerization (Figure 2b,c; Table S4) [29–31]. Macroscopically, this simulated network enhancement is supported by DSC analysis (Figure S19 and Note S5). Both T_g (865°C–992°C) and T_p (1057°C–1169°C) exhibit a synchronized, monotonic elevation as Al_2O_3 content increases, providing direct thermodynamic evidence for the rigidified aluminosilicate framework. Fourier-transform infrared (FTIR) spectroscopy confirmed that the network structure of the PGs predominantly comprises [SiO_4] and [AlO_4] tetrahedra (Figure 2d). Meanwhile, for GCs, distinct characteristic absorption peaks associated with Mg-O-Mg, Si-O, Si/Al six-membered rings and Si-O-Al (574, 622, 761, 945 cm^{-1}) are observed, corresponding to the precipitated MAS lattice (Table S5) [32–34]. Raman spectroscopy further elucidated the structural evolution, with peak fitting of the high-frequency region of PG revealing multiple $Si(OAl)_y$ units (Figure 2e, Figure S20, Note S6) [35–37]. Specifically, an increase in the Al/Si ratio led to a decrease in the proportions of $Si(OAl)_3$ and $Si(OAl)_4$ (Table S6), a redshift in the Raman peaks, and a decrease in the content of non-bridging oxygen (XPS O1s, Figure 2f) [38]. The aforementioned simulation and experimental results suggest that Al^{3+} functions as a network former to enhance the network's construction, degree of polymerization, and subsequent crystallization behavior [39]. To quantitatively evaluate the crystallization kinetics, the crystallization activation energy (E_c) was calculated via the Kissinger method (Figure S21, Note S7) [40]. The E_c value increases from 518 kJ/mol (PG20) to 644 kJ/mol (PG34), reflecting a heightened kinetic barrier stemming from the heavily cross-linked Q_4-dominated aluminosilicate glass framework. Crucially, this dynamic barrier works synergistically with the localized structural template to govern the crystallization. On one hand, this cordierite-like (Al/Si-rich) network acts as a structural topological template that effectively reduces the local thermodynamic nucleation barrier (Figure 2g), promoting highly oriented, pure-phase embryonic formation. Meanwhile, the higher E_c provides a rigid kinetic barrier that effectively suppresses random structural fluctuations and restricts the long-range diffusion and agglomeration of Eu^{2+}[41]. This unique kinetic-thermodynamic synergy successfully directs the atomic rearrangement of Si-O-Al-O-Si chains into the specific cyclic units of cordierite in a highly prioritized and controlled manner, thereby maximizing both the phase-pure crystallinity and the comprehensive luminescent performance (Figure 2h; Figures S22 and S23, Note S8).

While the aluminosilicate network gains macroscopic rigidity, this long-range structural change does not directly induce luminescence conversion but acts as a precursor to regulate local ordering during crystallization. Consequently, magic-angle spinning nuclear magnetic resonance (MAS-NMR) was employed to elucidate the local structural environment of MAS GCs and investigate the principles governing their structural evolution. As shown in Figure 3a, the ^{27}Al MAS-NMR spectra exhibit pronounced line broadening due to the quadrupolar nature of ^{27}Al and the structural disorder of the glass network, limiting the analysis to qualitative evaluation of Al coordination states. Nevertheless, the ~45 ppm [AlO_4] peak (deconvoluted into T1/T2 components) shows a clear increase in T1 intensity with increasing Al_2O_3 content. In comparison, upon in-situ crystallization, the amorphous broadening in the ^{29}Si MAS-NMR spectrum vanished entirely, revealing two distinct characteristic peaks, which can be fitted to decompose into Si(nAl) (n = 1–4) components (Figure 3b; Figure S24, Table S7) [42], with the relative content of each component provided in Table 1. Based on the fitting results, the Si/Al ratio, serving as an ordering parameter in cordierite, can be determined as follows [43]:

$$\frac{\mathrm{Si}}{\mathrm{Al}} = \sum_{n=0}^{4} \mathrm{ISi\,(nAl)} \Big/ \sum_{n=0}^{4} 0.25\mathrm{n\ Isi\,(nAl)} \quad (1)$$

where $\sum_{n=0}^{4} I\mathrm{Si}(n\mathrm{Al})$ denotes the integrated intensity of all sub-peaks in the ^{29}Si NMR spectra. The Si/Al ratios of GC20 and GC34 are 1.62 and 1.47, respectively, compared to 1.25 for natural cordierite, further evidence shows that the optimization of the amorphous network structure enhances the structural order of MAS: Eu^{2+} GCs. The Al/Si coordination occupancy at T1 and T2 sites can be precisely calculated, with quantitative analysis revealing that in GC34 (high Al_2O_3), T1 is dominated by Al (0.84Al:0.16Si) and T2 by Si (0.25Al:0.75Si), whereas in GC20 (low Al_2O_3), the distribution is reversed (T1: 0.21Al:0.79Si, T2: 0.66Al:0.34Si), demonstrating that Al_2O_3 content regulates the redistribution of Al and Si, thus expanding T1 and contracting T2 (Figure 3c; Note S9). Crucially, DFT calculations confirm that this local T1/T2 ordering drastically lowers the thermodynamic barrier for preferential Eu^{2+} migration into the interstitial six-membered rings. Driven by the Al^{3+}/Si^{4+} radius mismatch, this localized ordering induces an expansion of the ring channels and a concurrent contraction of neighboring [MgO_6] sites, effectively driving the larger Eu^{2+} activators into the ring positions as validated by Rietveld refinements (Figure 3d; Figure S25). Consequently, this structural reordering reconstructs the

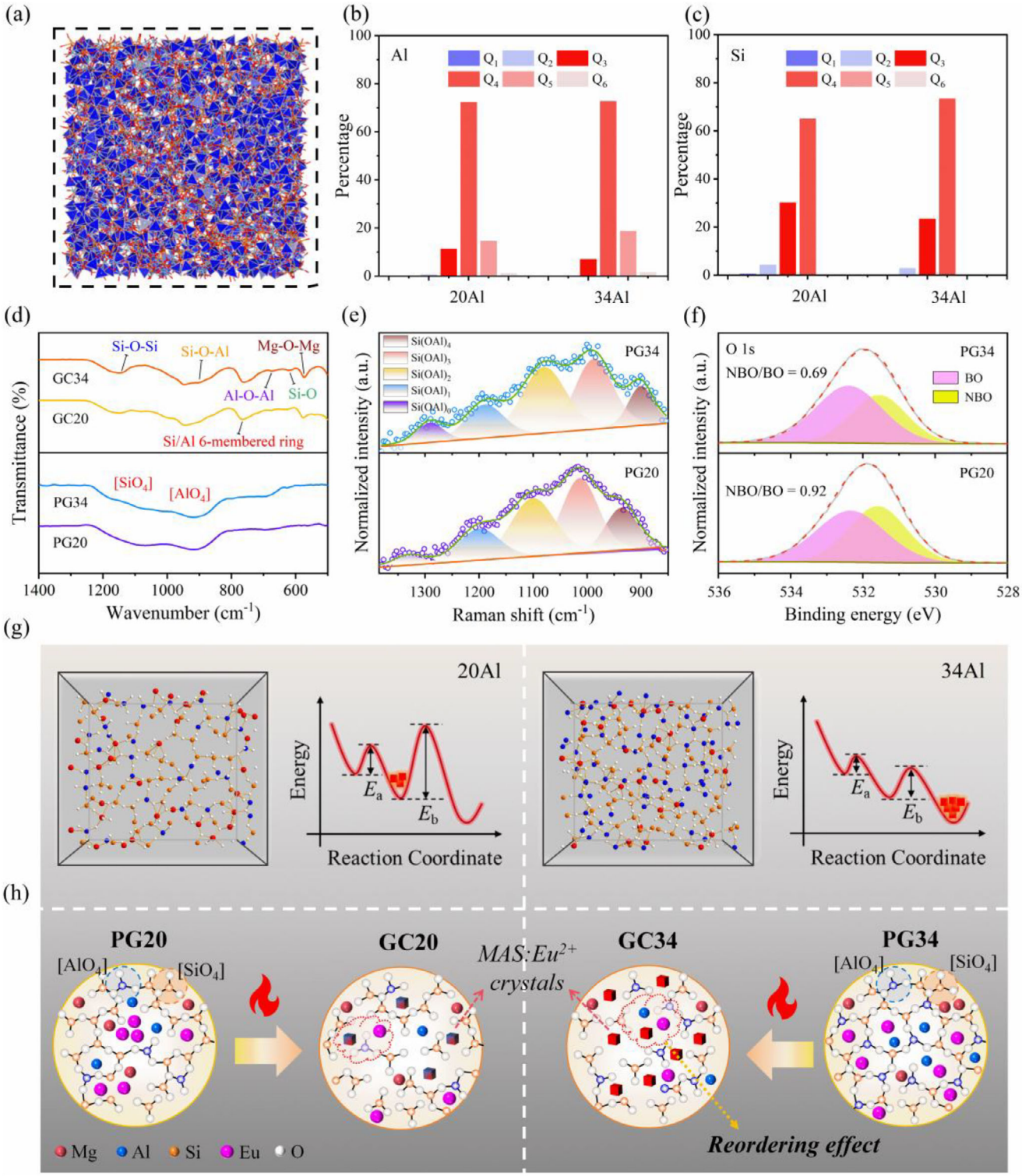

FIGURE 2 | Amorphous structure engineering and crystallization regulation of MAS: Eu^{2+} GCs. (a) Snapshot of the MD simulated glass structure. The percentages of Q_n ($n = 0–6$) coordination of (b) Al and (c) Si in simulated glass samples 20Al and 34Al. (d) FTIR spectra of PGs, GCs samples. (e) Deconvolution of the high-frequency band of Raman bands for PGs. (f) High-resolution XPS O1s spectra and deconvolution of PG samples. (g) The 3D models of 20Al and 34Al glasses obtained from MD simulations, together with the qualitative energetics of their chemical state evolution. (h) Schematic diagram of in-situ glass crystallization of MAS lattice induced by amorphous structure engineering.

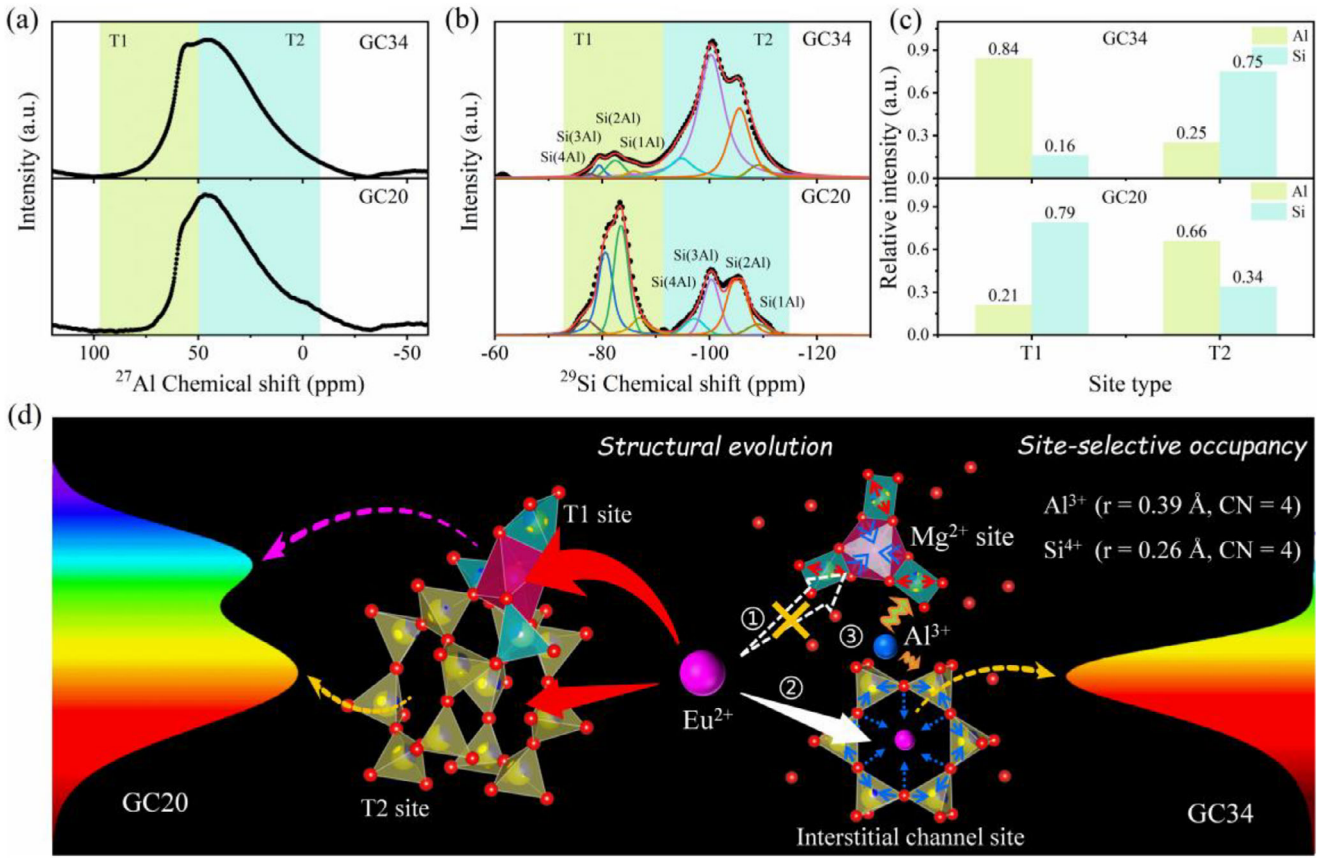

FIGURE 3 | MAS lattice evolution and Eu^{2+} ion site occupation transfer. (a) ^{27}Al, (b) ^{29}Si MAS-NMR spectra, and (c) relevant Al/Si ratio in the T1 and T2 sites of GC20 and GC34 samples. (d) Schematic diagram of structural evolution of the MAS lattice and site-selective occupancy of Eu^{2+}-activators.

TABLE 1 | Relative ratios of the deconvoluted Si(*n*Al) sub-peaks at the T1 and T2 sites.

	T1 site				T2 site					
	Si(4Al)	**Si(3Al)**	**Si(2Al)**	**Si(1Al)**	**Si(4Al)**	**Si(3Al)**	**Si(2Al)**	**Si(1Al)**	$\sum Si(nAl)_{T1}$	$\sum Si(nAl)_{T2}$
GC20	0.0427	0.2338	0.2489	0.0620	0.0493	0.1404	0.1893	0.0336	0.5874	0.4126
GC34	0.0071	0.0240	0.0425	0.0234	0.0915	0.5523	0.2255	0.0337	0.0970	0.9030

Eu-O coordination symmetry and tailors the crystal-field strength, causing a pronounced 5d level depression that directly triggers the sharp blue-to-red spectral switching.

2.3 | Performance Evaluation of Lighting Devices

Based on excitation from a violet LED chip, two types of full-spectra 1 W/10 W WLEDs were constructed using MAS: Eu^{2+} GCs as the core. The precise spectral regulation by red-emitting GCs enabled both devices to produce white light with warm correlated color temperature (CCT), high luminous efficiency, excellent CRI (>96.8), and R1–R15 values above 91 (Figure 4a–f). Variable-current electroluminescence (EL) and transient stable operational behavior under heat accumulation equilibrium confirm that due to the high thermal stability of MAS: Eu^{2+} red-emitting glass ceramic low- and high-power LEDs both maintain exceptional color temperature and CRI stability, underscoring its crucial role in achieving efficient and stable warm-color-temperature full-spectrum healthy lighting (Figure 4g–i, Figures S26 and S27), while acknowledging that comprehensive long-term reliability assessments (e.g., ≥ 1000 h) remain an essential objective for subsequent investigations.

Leveraging the broad excitation spectrum of MAS: Eu^{2+}, which enables efficient pumping by both violet and blue light, its blue laser-driven lighting performance was subsequently investigated. This lighting device was fabricated by screen-printing MAS: Eu^{2+} layers onto $Y_3Al_5O_{12}$: Ce^{3+} (YAG: Ce^{3+}) transparent ceramic substrates (Figure S28), followed by a test on its photometric/chromaticity parameters using a reflective-configuration laser-driven lighting test system (Figure 5a). As illustrated in Figure 5b, an increase in the MAS: Eu^{2+} GC content leads to an enhancement of the red emission component, resulting in a shift of the CIE 1931 chromaticity coordinates from cold white (0.2948, 0.3220) to warm white (0.3803, 0.3237). This alteration

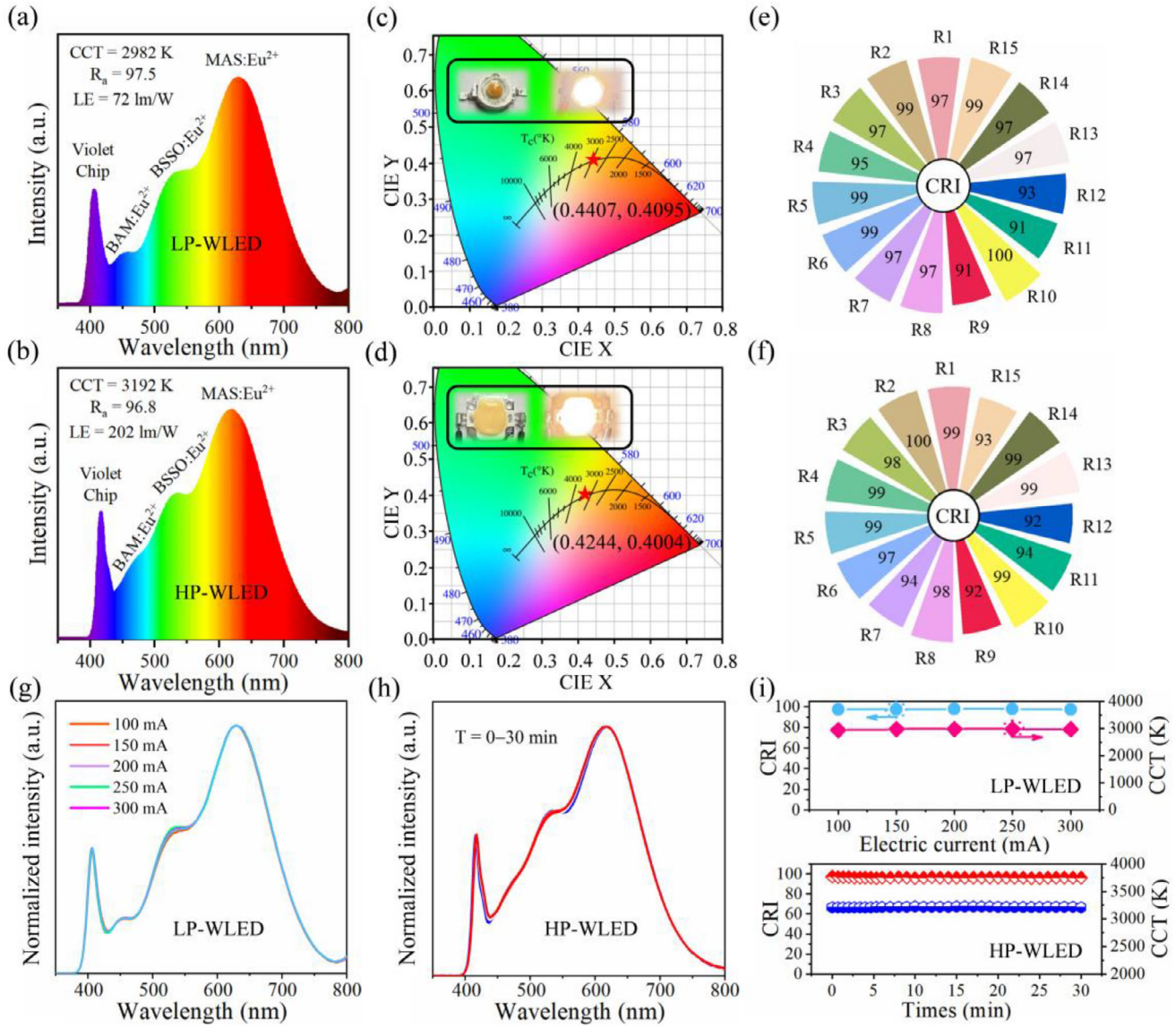

FIGURE 4 | Construction of high color rendering index WLED based on MAS: Eu^{2+} GCs. (a,b) EL spectra, (c,d) CIE 1931 chromaticity coordinates and (e,f) CRI of the prepared LP/HP-WLED devices. Normalized EL spectra of LP/HP-WLED devices at (g) different driving currents, (h) recorded within 30 min, and their corresponding (i) CRI and CCT values.

concurrently reduces the CCT from 7824 to 3708 K and elevates the CRI from 62.0 to 80.7, which significantly improves the quality of laser-driven lighting (Figure 5c,d). The optimized laser-driven lighting system, utilizing four layers of MAS: Eu^{2+} GC, achieves exceptional performance, with a CCT of 3708 K, CRI of 80.7, and a luminous efficacy (LE) of 240.3 lm/W_{opt} (Figure 5e). Due to the excellent thermal stability of MAS: Eu^{2+} GC, its luminous flux (LF) steadily increases with incident power, reaching a maximum of 619 lm at a saturation threshold of 25 W (9.77 W/mm^2) (Figure 5f). When illuminating multicolored objects, this optimized MAS: Eu^{2+} GC-based laser-driven lighting demonstrates superior color reproduction and visual clarity, offering more vivid and natural colors in comparison to lighting sources lacking MAS: Eu^{2+} GC (Figure 5g, Figure S29). Further, the lighting source exhibits excellent long-range illumination characteristics, making it suitable for applications such as automotive headlamps and projection lighting (Figure 5h–j), confirming that MAS: Eu^{2+} GC is a highly promising red-emitting color converter.

3 | Conclusions

In summary, high-performance red-emitting MAS: Eu^{2+} GCs were successfully developed through amorphous structure engineering. The reconstruction of the amorphous network via Al_2O_3 content modulation enhances the polymerization degree of the aluminosilicate glass and establishes a MAS-like topology, achieving an exceptional crystallinity of 98.2%. Concurrently, this strategy induces Al/Si lattice rearrangement, promoting the preferential occupation of interstitial channel sites by Eu^{2+} ions and enabling pure red emission centered at 620 nm. Due to the optimized Eu^{2+} site occupancy and improved structural order, the resulting MAS: Eu^{2+} GCs exhibit an ultrahigh IQE of 99.8% and remarkable thermal stability, with a luminescence decrease of only 7% at 425 K. These features render them highly suitable for high color-rendering and high-flux illumination applications in LEDs and blue-laser-driven lighting systems. This study demonstrates that MAS: Eu^{2+} GCs are promising candidates

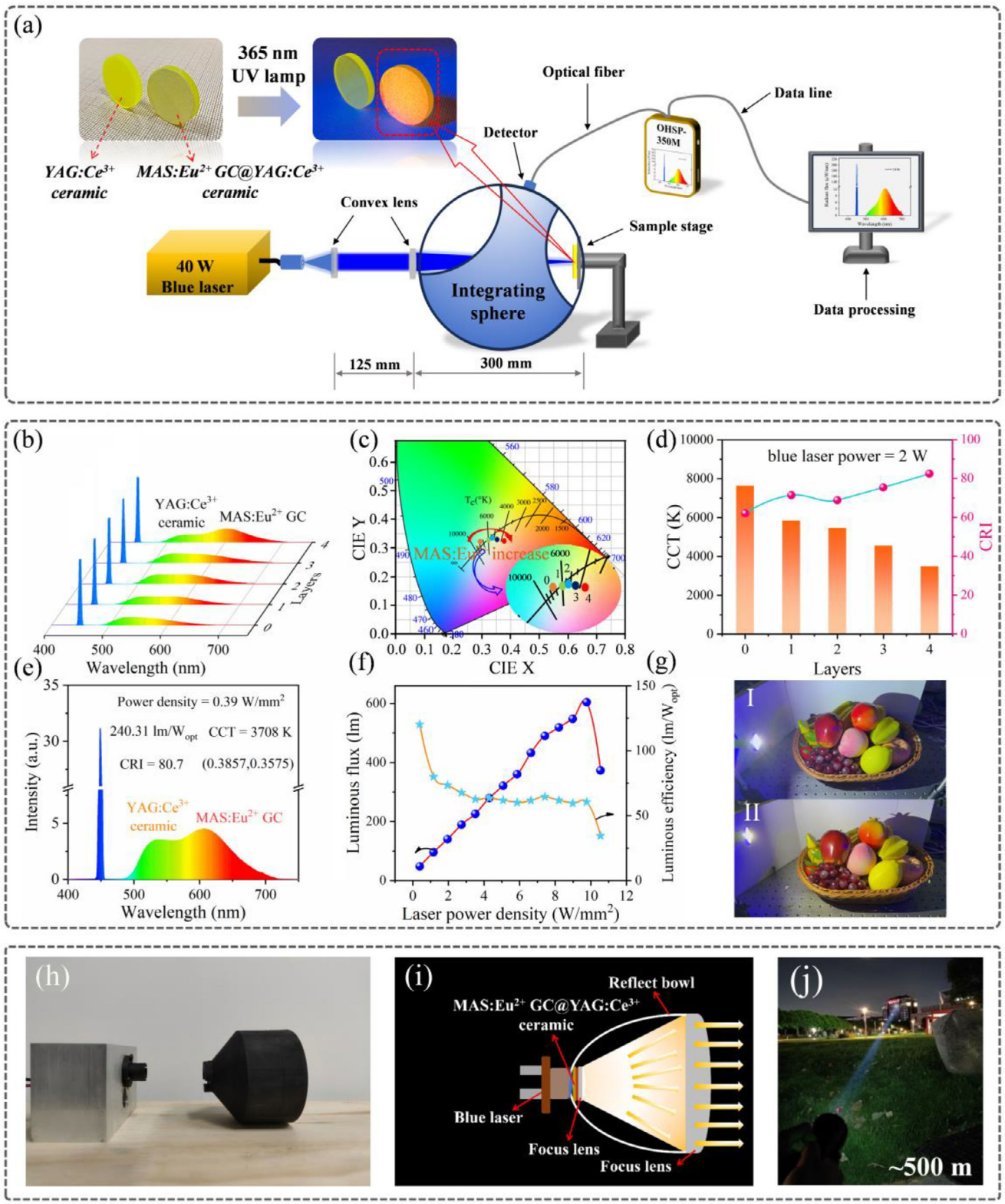

FIGURE 5 | The photoelectric characteristics of LD light-emitting devices driven by MAS: Eu^{2+} GCs (a) Schematic illustration of the laser-driven light source test system with reflective configuration. (b) Normalized EL spectra, (c) CIE 1931 chromaticity coordinates and (d) CRI and CCT of the WLD devices constructed with varying amounts of MAS: Eu^{2+} GC. (e) EL spectrum and related parameters of the optimized WLD device with 4 layers MAS: Eu^{2+} GC. (f) Pumping power-dependent LF and LE variations. (g) Photographs of fruits illuminated by the WLD devices with (I) 0 and (II) 4 layers MAS: Eu^{2+} GC. Photographs of the LD-driven prototype with (h) transmissive configuration, and its corresponding (i) optical systems and (j) illumination effects at night.

for high-quality SSL and provides valuable guidance for the design and development of high-performance red-emitting color converters for next-generation SSL technologies.

Acknowledgements

This research was supported by National Key Research and Development Program of China (2021YFB3500503), National Natural Science Foundation of China (52572155, 52272141, and 12304442), Natural Science Foundation of Fujian Province (2024J02014, 2024J01949), and Natural Science Foundation of Zhejiang Province (LY22E020008).

Conflicts of Interest

The authors declare no conflicts of interest.

Data Availability Statement

The data that support the findings of this study are available from the corresponding author upon reasonable request.

References

1. S. Hariyani, M. Sójka, A. Setlur, and J. Brgoch, "A Guide to Comprehensive Phosphor Discovery for Solid-state Lighting," *Nature Reviews Materials* 8 (2023): 759–775, https://doi.org/10.1038/s41578-023-00605-6.

2. M. Zhao, Y. Ge, Y. Li, X. Song, Z. Xia, and X. Zhang, "Suppressed Concentration Quenching and Tunable Photoluminescence in Eu^{2+}-Activated $Rb_3Y(PO_4)_2$ Phosphors for Full-Spectrum Lighting," *Light: Science & Applications* 13 (2024): 266, https://doi.org/10.1038/s41377-024-01607-x.

3. H. Zhang, H. Li, J. Li, et al., "Absolutely Structural Disorder Boosting Bandwidth Toward Full-Spectrum White Light From Single Occupancy of Activator," *Advanced Materials* 36 (2024): 2412099, https://doi.org/10.1002/adma.202412099.

4. P. Wang, Y. Wang, Z. Li, H. Wang, and T. Seto, "Enhanced Stability and Brightness Through Co-Substitution: Promoting Plant Growth With Green-Excited Deep Red Phosphor Ca 1-z Sr z Li 1-x Mg 2x Al 3-x N 4:YEu 2+," *Advanced Materials* 37 (2025): 2414578, https://doi.org/10.1002/adma.202414578.

5. J. Qiao, L. Ning, M. S. Molokeev, et al., "Site-Selective Occupancy of Eu 2+ Toward Blue-Light-Excited Red Emission in a Rb 3 YSi 2 O 7:Eu Phosphor," *Angewandte Chemie* 131 (2019): 11645–11650, https://doi.org/10.1002/ange.201905787.

6. Z. Li, H. Wang, Z. Su, R. Kang, T. Seto, and Y. Wang, "Enhanced Quantum Efficiency via Co-Substitution in Red-Emitting Phosphor Sr 2 [MgAl 5 N 7] : Eu 2+ for Advanced Spectroscopic Applications Including Laser Displays With Ultra-High Luminescence Saturation Threshold," *Angewandte Chemie* 137 (2025): 202419910, https://doi.org/10.1002/ange.202419910.

7. G. J. Hoerder, M. Seibald, D. Baumann, et al., "Sr[Li2Al2O2N2]:Eu2+—A High Performance Red Phosphor to Brighten the Future," *Nature Communications* 10 (2019): 1824, https://doi.org/10.1038/s41467-019-09632-w.

8. G. Liu, Y. Wang, and T. Seto, "A Giant Stokes Shift in Wide-Band Red Phosphor [Ca 0.33 (Sr 1-x Ba x) 0.67] 7 (SiO 3) 6 Cl 2: Eu 2+-Band Red Phosphor [Ca0.33(Sr1-xBax)0.67]7(SiO3)6Cl2: Eu2+," *Advanced Optical Materials* 12 (2024): 2303189, https://doi.org/10.1002/adom.202303189.

9. Y. Kuang, J. Jin, G. Liu, W. Chen, and Z. Xia, "KBaScSi 3 O 9:Eu 2+ Glass-Ceramics as Single-Phase High-Power White Emitters," *Advanced Functional Materials* 35 (2025): 2418751, https://doi.org/10.1002/adfm.202418751.

10. S. Zhu, S. Jin, L. Zhan, et al., "Glass Network Engineering of Yellow-Emitting $Ba_2Sc_2B_4O_{11}$: Ce^{3+} Glass Ceramics for Full-Spectrum Lighting," *Journal of Advanced Ceramics* 14 (2025): 9221169, https://doi.org/10.26599/JAC.2025.9221169.

11. Y. Sun, X. Zhou, Z. Lun, K. Han, P. Xiong, and Z. Xia, "Amorphous to Crystalline Phase Transformation Enables Tunable Persistent Luminescence for Multi-Mode Optical Information Storage," *Advanced Functional Materials* 34 (2024): 2406336, https://doi.org/10.1002/adfm.202406336.

12. Y. Zhu, G. Tang, Z. Hua, et al., "Color Tunable Emission and Scintillation Properties of Eu-Doped Lanthanum Alumino-Silicate Glasses," *Journal of Rare Earths* 43 (2024): 2385–2394, https://doi.org/10.1016/j.jre.2024.11.018.

13. J. Chen, Q. Su, J. Zou, et al., "Blue-Cyan Emitting Eu^{2+}-Doped Oxyfluoride Glass for X-Ray Scintillator and White LED," *Laser & Photonics Reviews* 20 (2026): e70981, https://doi.org/10.1002/lpor.70981.

14. R. Tian, Q. Wang, S. Li, T. Zhou, and R.-J. Xie, "Efficient $Sr_{0.5}Ca_{0.5}AlSiN_3$: Eu^{2+} Red-Emitting Ceramics for High-Power Solid-State Lighting," *Journal of Materials Science & Technology* 210 (2025): 179–187, https://doi.org/10.1016/j.jmst.2024.04.079.

15. T. Hu, Y. Guo, X. Yi, M. Zhao, Y. Gao, and H. Lin, "Integrated Multi-Responsive $SrMg_2Al_6Si_9O_{30}$: Eu^{2+} Osumilite Glass Ceramic via in Situ Crystallization: A Unified Platform for Smart Optical Applications," *Advanced Functional Materials* 36, no. 33 (2026): 31457, https://doi.org/10.1002/adfm.202531457.

16. J. Zhao, L. Lei, R. Ye, J. Zhang, X. Zhang, and S. Xu, "Sunlight Activated Ultra-Stable Long Persistent Luminescence Glass Ceramic for Outdoor Information Display," *Journal of Advanced Ceramics* 11 (2022): 974–983, https://doi.org/10.1007/s40145-022-0595-1.

17. X. Zou, H. Zhang, W. Li, et al., "Ultra-Wide Vis–NIR Mg 2 Al 4 Si 5 O 18:Eu 2+ ,Cr 3+ Phosphor Containing Unusual NIR Luminescence Induced by Cr 3+ Occupying Tetrahedral Coordination for Hyperspectral Imaging," *Advanced Optical Materials* 10 (2022): 2200882, https://doi.org/10.1002/adom.202200882.

18. R. Zhou, D. Hua, B. Liu, et al., "RGB-Tricolor Multimodal Luminescence of Ce^{3+} and Mn^{2+} in $Mg_2Al_4Si_5O_{18}$ via Site Occupancy Engineering for Anticounterfeiting Applications," *Materials Today Chemistry* 40 (2024): 102287, https://doi.org/10.1016/j.mtchem.2024.102287.

19. M. T. Dove and L. Li, "Anomalous Thermal Expansion of Cordierite, Mg2Al4Si5O18, Understood Through Lattice Simulations," *Matter* 8 (2025): 101943.

20. T. Hu, L. Ning, Y. Gao, et al., "Glass Crystallization Making Red Phosphor for High-Power Warm White Lighting," *Light: Science & Applications* 10 (2021): 56, https://doi.org/10.1038/s41377-021-00498-6.

21. W. Zhu, Z. Zhang, W. Deng, J. Liu, F. Cao, and X. Shen, "Luminescent Structure Evolution Triggered White Emission in α-$Mg_2Al_4Si_5O_{18}$: Eu^{2+} Through Eu^{2+} Occupancy Induced by Al^{3+} Content/B^{3+}-P^{5+} Double Substitution," *Journal of Rare Earths* 43 (2025): 888–899, https://doi.org/10.1016/j.jre.2024.05.005.

22. K. Song, H. Yu, Q. Nie, et al., "Synthesis and Luminescence Characteristics of $Mg_2Al_4Si_5O_{18}$: Eu^{2+} and Nitrided $Mg_2Al_4Si_5O_{18}$: Eu^{2+} Phosphors," *Journal of Luminescence* 224 (2020): 117317, https://doi.org/10.1016/j.jlumin.2020.117317.

23. D. Stefańska and P. J. Dereń, "High Efficiency Emission of Eu^{2+} Located in Channel and Mg-Site of $Mg_2Al_4Si_5O_{18}$ Cordierite and Its Potential as a Bi-Functional Phosphor Toward Optical Thermometer and White LED Application," *Advanced Optical Materials* 8 (2020): 2001143.

24. W. Höland and G. H. Beall, *Glass-ceramic Technology* (Wiley Online Library, 2012).

25. H. Tong, H. Li, W. Liu, and G. Ouyang, "Lead-Free Organic Antimony Halide With Dual-Band Intrinsic White Light Emission for Warm WLED Directly," *Chinese Journal of Structural Chemistry* 44 (2025): 100678.

26. H. Takahashi and Y. Matsushima, "Luminescent Properties of RE-Doped Mullite (Al 6 Si 2 O 13) Phosphors(RE = Ce 3+ , Eu 2+ , Ce 3+ -Tb 3+ , and Eu 3+), Eu2+, Ce3+-Tb3+, and Eu3+)," *ECS Transactions* 88 (2018): 237–247, https://doi.org/10.1149/08801.0237ecst.

27. S. Chen, J. Lin, J. Huang, et al., "CsPbBr 3 @Glass Nanocomposite With Green-Emitting External Quantum Efficiency of 75% for Backlit Display," *Advanced Functional Materials* 34 (2024): 2309293, https://doi.org/10.1002/adfm.202309293.

28. J. He, R. Shi, Z. Wang, M. Li, T.-K. Sham, and L. Fu, "Suppression of Eu^{2+} Luminescence Loss," *Advanced Optical Materials* 10 (2022): 2101751, https://doi.org/10.1002/adom.202101751.

29. X. Xu, J. Zhao, X. Chen, et al., "Ca 2+ /Sr 2+ /Ba 2+ Dependent Phase Separation, Nanocrystallization and Photoluminescence in Fluoroaluminosilicate Glass," *Journal of the American Ceramic Society* 103 (2020): 5796–5807, https://doi.org/10.1111/jace.17299.

30. T. Hu, H. Yang, Y. Guo, J. Huang, Y. Gao, and H. Lin, "Eu 2+ Doping Driven Polymorphic Transition in Sr 2 SiO 4 Glass Ceramic for Optical Property Tailoring and Multifunctional Photonic Applications," *Advanced Optical Materials* 13 (2025): 01563, https://doi.org/10.1002/adom.202501563.

31. Z. Pan, Z. Qin, M. Zhu, et al., "Thermal-Robust and Glass-Compatible $K_{1.3}Al_9Ga_2O_{17.15}$: Eu for Laser-Driven Lighting and Underwater Optical Communication," *Laser & Photonics Reviews* 20, no. 5 (2025): 02372, https://doi.org/10.1002/lpor.202502372.

32. M. Li, G. Xu, J. Dong, et al., "Effect of Substituting Li2O With ZnO on the Crystallization and Properties of Li2O–Al2O3–SiO2 Transparent Glass Ceramics," *Ceramics International* 50 (2024): 24521–24530, https://doi.org/10.1016/j.ceramint.2024.04.187.

33. Z. Bao, X. Wang, W. Luo, S. Wang, and L. Miao, "A Novel Transparent Glass-Ceramic With the Crystallization of $Mg_{0.6}Al_{1.2}Si_{1.8}O_6$ From MgO-Al_2O_3-SiO_2 System Without Adding Nucleating Agents," *Ceramics International* 51 (2025): 6824–6834, https://doi.org/10.1016/j.ceramint.2024.12.114.

34. J. Song, Z. Zhou, B. Zhong, M. Zhang, J. Huang, and L. Han, "Ultra-Broadband Near-Infrared Cr^{3+}-doped Multi-Phase Glass-Ceramics Realized by the Selective Enrichment Strategy for Near-Infrared Spectroscopy Applications," *Journal of Alloys and Compounds* 968 (2023): 172126, https://doi.org/10.1016/j.jallcom.2023.172126.

35. W. Yu, S. Cao, J. Wang, et al., "Crystallization Mechanisms of Cordierite Glass-Ceramics With "Surface-Center" Crystallization Behavior," *Journal of the European Ceramic Society* 41 (2021): 6708–6721, https://doi.org/10.1016/j.jeurceramsoc.2021.05.061.

36. P. McMillan, B. Piriou, and A. Navrotsky, "A Raman Spectroscopic Study of Glasses Along the Joins Silica-Calcium Aluminate, Silica-Sodium Aluminate, and Silica-Potassium Aluminate," *Geochimica et Cosmochimica Acta* 46 (1982): 2021–2037, https://doi.org/10.1016/0016-7037(82)90182-X.

37. D. R. Neuville, L. Cormier, V. Montouillout, et al., "Amorphous Materials: Properties, Structure, and Durability: Structure of Mg- and Mg/Ca aluminosilicate Glasses: 27Al NMR and Raman Spectroscopy Investigations," *American Mineralogist* 93 (2008): 1721–1731, https://doi.org/10.2138/am.2008.2867.

38. C. Chen, W. Li, C. Ni, and W. Dai, "Manganese Valence Modulation in $ZnGa_2O_4$ via Simultaneously Localized Charge Accumulation and Oxygen Vacancy Engineering Controlled by Li^+ and F^- Substitutions for Tailored Applications," *Chinese Journal of Structural Chemistry* 45, no. 5 (2026): 100868, https://doi.org/10.1016/j.cjsc.2026.100868.

39. T. Pang, S. Lin, F. You, et al., "Synergistic Enhancement of Crystallinity and Transparency in Tb^{3+}-Doped Nano-Glass-Ceramics for High-Resolution X-Ray Imaging," *Journal of Advanced Ceramics* 14 (2025): 9221122, https://doi.org/10.26599/JAC.2025.9221122.

40. S. Lin, H. Lin, H. Yang, et al., "Highly Crystalline $Y_3Al_5O_{12}$:Ce^{3+} Phosphor-in-Silica Glass Ceramics for High-Power Solid-State Lighting," *Journal of Rare Earths* 42 (2024): 2051–2057, https://doi.org/10.1016/j.jre.2023.09.011.

41. X. Li, C. Yang, L. Qiu, et al., "NaAlSiO 4: Eu 2+ Glass Ceramics: Self-Reduced In Situ Growth and High-Power LED/LD Lighting," *Laser & Photonics Reviews* 16 (2022): 2100346, https://doi.org/10.1002/lpor.202100346.

42. W. Chen, Y. Wang, G. Liu, Y. Sun, and Z. Xia, "Si/Al Order and Texture Orientation Optimization of Red-Emitting $Mg_2Al_4Si_5O_{18}$: Eu^{2+} Ceramics for Laser Phosphor Display," *Journal of Materiomics* 10 (2024): 1137–1143, https://doi.org/10.1016/j.jmat.2024.02.001.

43. J. Senegas, A. R. Grimmer, D. Muller, P. Thomas, D. Mercurio, and B. Frint, "Determination of the Al/Si Distribution in Synthetic $K_xMg_2Al_{4+x}Si_{5-x}O_{18}$ ($0<x\leq1$) Cordierites by ^{29}Si and ^{27}Al MAS-NMR Spectroscopy," *Journal of Materials Science* 26 (1991): 5053–5059.

Supporting Information

Additional supporting information can be found online in the Supporting Information section.

Supporting File: adfm76844-sup-0001-SuppMat.docx.